

# Security Analysis of Camera-LiDAR Semantic-Level Fusion Against Black-Box Attacks on Autonomous Vehicles

R. Spencer Hallyburton  
Duke University

Yupei Liu  
Duke University

Miroslav Pajic  
Duke University

## Abstract

To enable safe and reliable decision-making, autonomous vehicles (AVs) feed sensor data to *perception* algorithms to understand the environment. Sensor fusion, and particularly semantic fusion, with multi-frame tracking is becoming increasingly popular for detecting 3D objects. Recently, it was shown that LiDAR-based perception built on deep neural networks is vulnerable to LiDAR spoofing attacks. Thus, in this work, we perform the first analysis of camera-LiDAR fusion under spoofing attacks and the first security analysis of semantic fusion in any AV context. We find first that fusion is more successful than existing defenses at guarding against naive spoofing. However, we then define the *frustum attack* as a new class of attacks on AVs and find that semantic camera-LiDAR fusion exhibits widespread vulnerability to frustum attacks with between 70% and 90% success against target models. Importantly, the attacker needs less than 20 random spoof points on average for successful attacks – an order of magnitude less than established maximum capability. Finally, we are the first to analyze the longitudinal impact of perception attacks by showing the impact of multi-frame attacks.

## 1 Introduction

Autonomous vehicles (AVs) have enjoyed millions of miles of partially automated road travel [4, 17, 26]. Perception is a fundamental element of autonomy, the foundation of safe and reliable decision-making. Sensors including cameras and light detection and ranging (LiDAR) collect the data for perception which provides AVs an awareness of surroundings; enabling informed decisions for safety-critical tasks such as obstacle and pedestrian avoidance, and lane and traffic sign detection.

The camera and LiDAR are the most used AV sensors [1–3, 18]. Inexpensive, high-quality cameras can provide high resolution, dense 2D outputs on limited fields of view. LiDAR is complementary to the camera, providing 360° view of the surroundings and fully resolving the 3D position of objects with a sparse set of points (i.e., point clouds).

Due to AVs’ safety-critical nature, misinformation or wrong decisions can quickly lead to severe adverse out-

comes [22, 36], highlighting the need for security research in this domain. In particular, the increasing reliance of AVs on deep neural networks (DNNs) for real-time perception has sparked security questions at the algorithm level. There is a growing body of AV security work; for perception algorithms, an attacker can perturb sensor data to change object classification (i.e., resulting in misclassification) [13], introduce fake objects (i.e., false positive) [8, 40], and remove existing objects (i.e., false negative) [5, 41], each with devastating consequences at the driving decision and control level.

Initially, security analysis of perception focused on the image domain, with LiDAR only recently emerging as the target for security research. Physically-realizable attacks against LiDAR have since been demonstrated [8, 33, 38, 40], as well as applied to LiDAR (only)-based perception systems [8, 40].

However existing security analyses of LiDAR-based perception have several limitations. From the perspective of the attack impact on autonomous driving, the existing works with physically-realizable attacks only consider single-sensor (e.g., LiDAR-only, camera-only) architectures on a single frame of data – i.e., no attacks over time (longitudinal attacks) and their impact are considered. Contrarily, deployed AV architectures such as Waymo’s One [26], Baidu’s Apollo [2], and NVIDIA’s DRIVE [3] make clear that multiple sensors should feed the perception pipeline to, along with multi-frame tracking, enhance perception robustness.

Consequently, in this work, we *present the first security analysis for camera-LiDAR sensor fusion under physically-realizable LiDAR spoofing attacks*. To put to rest LiDAR-only perception, we first revisit the leading defense against attacks on LiDAR-only perception [40]; CARLO was shown to guard perception against *false positive* (FP) attacks that introduce fake vehicles in front-near positions in near-real-time [40]. We demonstrate that CARLO is not capable of guarding against FP injections outside of front-near and that the defense itself introduces vulnerabilities to *false negative* (FN) attacks that ‘remove’ existing vehicles. This shows that with no other promising model-agnostic defenses and inferior baseline performance to fusion (e.g., [42] vs. [25]), LiDAR-only percep-

tion has limited promise in adversarial environments.

We then analyze fusion, and specifically, semantic camera-LiDAR fusion, as opposed to fusion at the feature-level, since semantic fusion is prevalent in AV industry, including Baidu Apollo [2] and NVIDIA DRIVE [3]. Furthermore, semantic fusion is a more modular counterpart to fusion at the feature-level, as detection pipelines can be isolated from one another and more easily interchanged [21]. Semantic fusion also reduces model parameters by mitigating the curse of dimensionality of the input space, thus reducing DNN sizes [20, 21].

We first show that *semantic fusion confers additional robustness against existing LiDAR attacks*; traditional, naive FP and FN attacks are intrinsically limited against certain fusion architectures. In fact, we leverage that naive LiDAR attacks on camera-LiDAR fusion generate inconsistencies between the camera and LiDAR sensor data to outline a lightweight cascaded camera-LiDAR defense framework that processes sensor data sequentially and eliminates nearly all ( $> 99\%$ ) FP attacks from the state-of-the-art attack introduced in [40].

Despite fusion’s increased robustness to naive FP and FN attacks, we introduce a new class of perception attacks, the *frustum attacks*, which are able to evade the camera-LiDAR defense framework by preserving semantic consistencies between the camera and LiDAR data. With only simple modifications to existing attacker knowledge — knowing approximate locations of true objects in the scene — we design a frustum attack that *is no longer detectable by the camera-LiDAR defense framework nor is it detectable by CARLO*. We apply the frustum attack to two widely-used semantic fusion algorithms: the Frustum PointNet (FPN) [34], a benchmark semantic fusion algorithm, and the Frustum ConvNet (FCN) [44]; these primarily differ in that FPN enforces detection of only one object per image proposal while FCN uses additional convolutional layers and allows for multiple detected objects per image proposal. For FPN, we show vulnerability to *translation of the detected object* using a frustum attack behind the targeted object, whereas FCN has widespread vulnerability to FP outcomes in front and behind the targeted object. Hence, we are the first to *demonstrate the vulnerability of camera-LiDAR semantic fusion to LiDAR spoofing attacks*.

We also improve feasibility of LiDAR-based attacks with two key results. First, we show that a LiDAR spoofing attack, without manipulating the camera feed, is sufficient for widespread attack success against fusion. Second, we show that a key assumption about the required attacker’s capabilities from prior work can be significantly relaxed. Specifically, while spoofed LiDAR points were accepted along an AV’s LiDAR channel in the lab [8, 33, 38, 40], when passing these points to perception for object detection, there was no success of generating FP or FN outcomes [8]. Existing spoofing attacks have only had success at creating FPs or FNs with precise placement of points; furthermore, existing LiDAR spoofing attacks have required either white-box model access [8] or carefully-crafted point placements in the outline of

real vehicles (e.g., adversary uses a dataset of cars [40]). With an in-depth security analysis of the fusion methods, we establish that *inserting a random sample of normally-distributed points is nearly as successful as inserting points in the outline of a car*. This confers inherent attack robustness to small perturbations, facilitating attack deployment with a physical spoofing device (e.g., [8, 33, 38]).

Furthermore, we systematically evaluate the frustum attack with FP, FN, and translation (i.e., ‘moving’ the detected object with simultaneous FP and FN, see Section 3.1) outcomes on camera-LiDAR fusion; we find that, out of instances from the KITTI dataset [14] with strong baseline performance (see Section 5.2), *70% are vulnerable to frustum attack with detection translation outcomes when FPN is used, while 90% and 25% of instances are vulnerable to FP-only and detection translation outcomes when FCN is used*. Also, frustum attacks on FPN are only successful behind targeted objects while attacks on FCN are successful both in front and behind targeted objects; this disparity is due to FPN allowing only a single 3D object detection per image proposal region whereas FCN allows multiple objects detected per image proposal region.

In addition, there is a wide margin of positions to insert spoofed points for successful attacks against both FPN and FCN; e.g., on average for each vulnerable case against FPN, the attacker has a window 10 *m* long where a cluster of points could be placed for successful attack. We find a surprising amount of generalization of the frustum attack – in each set of parameters studied, *attack success rate against both FPN and FCN always peaks near a spoof point injection distance of 9 m post-target*. Even if the attacker is blind to the best choice of parameters for each instance and must select *a priori* parameters for all attacks, he can still achieve 80% and 92% success against FPN, and 87% and 96% success against FCN targeting vehicles 25 *m* and 35 *m* from the host, respectively. To make matters worse, we show that the attacker needs to insert less than 20 points on average for successful attack on all vulnerable instances, an *order of magnitude less* than the established maximum capability.

Finally, to assess the impact LiDAR attacks could have on AVs equipped with multi-frame tracking, we present *the first security studies considering longitudinal (i.e., over time) sequences of perception data*. Deployed AVs leverage multiple frames to estimate (and track) vehicle kinematics, filter false positives, and build resiliency to false negatives [2, 3, 17]. When considering detection translation outcomes, although translating the detected position of a car might not seem like an effective attack, we show that it can have significant consequences if exercised over time. While previous studies [8, 40] required FPs at close distance ( $< 10$  *m*) from the host for high-impact, we demonstrate that high-impact (i.e., endangering vehicle safety) adversarial situations occur even when attacking at a longer range by attacking over multiple time points; effectively deceiving the host vehicle’s tracking and control.

In summary, we make the following contributions:

- We show that existing defenses against established black-box LiDAR-based attacks fail to defend perception, whereas multi-sensor fusion reduces attack success rate to below 1% over the entire attack space.
- We perform the first security analysis of multi-sensor fusion AV algorithms under experimentally demonstrated attacks. We find that existing attacks are insufficient to exploit sensor fusion vulnerabilities and establish the *frustum attack*. We further establish the *translation outcome* as a hybrid between FP and FN outcomes. We improve feasibility of spoofing attacks by *i)* showing that similar success is achieved with random samples of normally-distributed spoof points compared to carefully patterned injections, and *ii)* on average, successful attacks need an order of magnitude fewer spoof points compared to the maximum established spoofing capability.
- We find widespread ( $> 70\%$  using FPN and  $> 90\%$  using FCN) vulnerability of fusion to the frustum attack. With perception algorithms enforcing one object detection per image proposal (e.g., FPN), successful frustum attacks always lead to translation outcomes but have more resiliency to attack placement. With multiple detections allowed per image proposal (e.g., FCN), frustum attacks are more resilient to translation outcomes, but are more susceptible to FP attacks overall, including attacks in front of the target, leading to devastating outcomes.
- We perform the first longitudinal studies of security against perception attacks over time sequences. We show that the attacker achieves high-impact outcomes even attacking at long range compared to previous short-range attack cases by using translation attacks to fool the vehicle’s tracking and control.

## 2 Background and Related Work

### 2.1 Perception

AVs interact in complex environments with active agents and dynamic weather and terrain situations. To accomplish desired tasks while retaining consistent situational awareness, deployed AVs are equipped with multiple sensors of multiple modalities, as well as perception algorithms to translate the sensor data into meaningful semantic information used to develop accurate situation awareness (e.g., vehicle tracking).

#### 2.1.1 Camera and LiDAR Sensing

AVs are equipped with multiple cameras spaced around the vehicle. Individual cameras provide monocular vision which resolve azimuth and elevation angles to targets. Cameras are inexpensive compared to active LiDAR and radars, and thus are the preferred sensing modality for AVs [2, 3, 14, 18].

In AV applications, a central LiDAR is commonly mounted on the vehicle roof for maximum viewing opportunity. LiDAR is complementary to the camera; it is an active sensor that sends primarily infrared light and constructs transmit-receive time differences to resolve the full 3D position of objects [18].

LiDAR has demonstrated enhanced robustness to adverse weather situations compared to cameras [24].

#### 2.1.2 KITTI Benchmark

We use KITTI [14] to test our algorithms and attacks. KITTI is composed of synchronized camera and LiDAR captures with ground truth 2D and 3D bounding boxes, and is divided into a trainval split of 7481 samples. We use the standard split of the trainval [9] into 3712 samples for algorithm training and 3769 samples to test our attacks. KITTI uses average precision (AP) under PASCAL [12] as the 3D object detection benchmark and only considers detections as true positive during evaluation with a  $> 70\%$  *bounding box overlap* (i.e., *Intersection over Union – IoU*). We use perception algorithms with publicly available models pretrained on KITTI to test our attacks.

#### 2.1.3 Perception Algorithms

The DNN resurgence has spawned unprecedented growth in camera-based perception tasks, including detection (e.g., [15, 29]), semantic segmentation (e.g., [11]), and pose estimation (e.g., [30]). Recently, novel techniques have been proposed for ingesting and operating on point cloud data from LiDAR. Three general classes of LiDAR-based perception include the bird’s-eye view (BEV) (e.g., [28]), voxelization of the 3D space (e.g., [45]), and direct ingesting of points (e.g., [37]). These early works focused on single-sensor perception pipelines without considering multi-sensor fusion.

Architectures and algorithms for sensor fusion have recently been developed to handle data from multiple sensors, improving perception performance (e.g., [42] vs. [25]). There are two broad classes of sensor fusion architectures: 1) fusion at the semantic level (e.g., [34, 42, 44]), and 2) fusion at the data/feature level (e.g., [10, 23]). Of a particularly high level of adoption are cascaded semantic fusion architectures that process one or more sensors in isolation and then fuse the high-level semantic information. This approach is widely used across industry and is employed by two of the largest open-source providers, Baidu Apollo [2] and NVIDIA DRIVE [3].

Consequently, in this work, we analyze security of semantic fusion due to its high degree of performance and proliferation. Specifically, we focus on the AV context and *perform security analysis of sensor fusion under experimentally demonstrated LiDAR spoofing attacks*. We ignore attacking the camera, as we find that attacking LiDAR alone is enough to significantly disrupt the fusion, effectively jeopardizing safety of the AVs.

**Frustum PointNet (FPN).** As a target perception algorithm, we consider FPN [34], a widely-used benchmark for evaluating new perception algorithms (e.g., [23, 37, 39]). Fig. 1 illustrates the data flow in FPN while Fig. 2 shows an example of its two-stage pipeline operating on an RGB image + 3D point-cloud instance from KITTI. FPN exploits mature 2D object detection using detections from the camera’s front-view image to extend a frustum proposal in 3D space. The camera detector also provides object class information (e.g., car, truck,

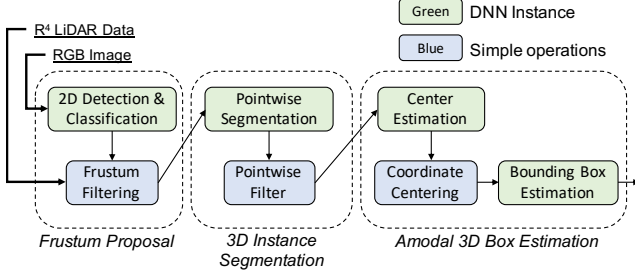


Figure 1: Each stage of FPN is built on DNN foundations. FPN uses a multi-sensor framework, ingesting an RGB image for classification and 2D detection, and filtering LiDAR points by extruding 2D detection to frustum. Instance segmentation identifies points relevant to the object of interest within the frustum. Final stage regresses a bounding box.

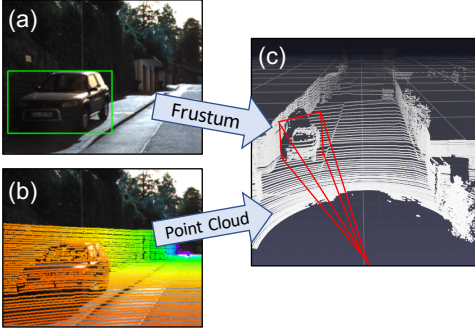


Figure 2: 2D detections from an RGB input (in (a) green box) extrude a frustum when projected along range (red frustum in (c)), allowing filtering of the LiDAR point cloud (in (b), color with depth; (c), grayscale with depth). FPN and FCN are two-stage semantic fusion algorithms (i.e., cascaded fusion).

pedestrian) to LiDAR processing. FPN uses a PointNet [35] to regress a bounding box within the frustum.

**Frustum ConvNet (FCN).** We also consider FCN [44] as a target perception algorithm with a similar two-stage approach of Fig. 2. FCN similarly leverages mature 2D camera-based detection to extrude a frustum in 3D space from region proposals. However, it differs from FPN by using convolution layers to operate on sub-regions within the frustum proposal, enabling it to output multiple objects per a single 2D camera-based detection.

## 2.2 Attacks on Perception

**Attacks on camera-based perception.** Camera-based perception algorithms that use DNN models have been shown vulnerable to black-box attacks (e.g., [32]). Attacks on camera-based perception have been extended to AV-specific contexts [7, 13], showing that object detection and classification are vulnerable when using only camera data.

**Demonstrations of LiDAR spoofing attacks.** Recently, [8, 33, 38, 40] have demonstrated feasibility of LiDAR spoofing devices. A relay system where LiDAR pulses were re-

ceived by a photodiode and relayed through an attack laser was introduced in [33]; the system was later expanded to control the 3D positioning of spoof points with a delay component [38], capitalizing on the regular patterning of LiDAR emissions. With this foundation, [8] established a 60 point stable spoofing baseline on a per-frame basis, subsequently improved to 200 points [40]. See Appendix A for more details.

**Attacks on point cloud detection.** Attacks on point cloud data have been recently extended to the AV context. Samples of 60 and 200 spoofed LiDAR points were shown to be accepted along the AV’s LiDAR channel in the lab [8, 40]. However, passing those spoofed points to perception for object detection has yielded minimal successful spoofed objects [8, 40]. Hence, [8] pivoted to appending spoof points online and considered placement of spoof points as a white-box optimization problem. In [40], black-box attacks are introduced, exploiting that DNNs may not encode causality about the data (e.g., occluded objects). Similarly, minimal success is seen in obtaining spoof detections after laboratory-generated spoofed points are passed to perception [40]. Thus, [40] also pivots to extracting valid occluded objects from KITTI, translating points to an attacker-desired location, and injecting them.

Furthermore, [5, 41, 43] introduce attacks with adversarial patches and mesh objects that are optimized for color, shape, and texture, and digitally rendered into LiDAR and/or camera. Each attack performs optimization either over training data [5, 41] or with white-box model access [43]. However, the adversarial meshes may be too large to be physically realized outside of a fully-cyber context, and attacks are only evaluated on a single frame of data. Finally, [41] illustrates that universal AV patch attacks are fragile, as their attack does not transfer between AV datasets.

For defenses against point cloud attacks on 3D object detection, [40] introduced 1) CARLO - an empirical defense for binary classification between valid and invalid instances, and 2) SVF - a re-architecting of the perception model with multi-view projection, similar to [10], while [16] casts detecting spoof objects as a binary classification problem using the shadow region behind detections for features.

**Translation attack.** Finally, the translation attack in a fully cyber context is introduced in [19] where publish/subscribe over-privilege allowed an attacker to directly manipulate message fields, in order to move (i.e., translate) the objects detected by perception from one location to another.

## 3 Attack Objectives and Threat Model

### 3.1 Attack Goals

We consider false positive (FP) and false negative (FN) attack outcomes consistent with the literature [8, 40, 41], as well as *translation attack outcomes* where a detected object’s bounding box is translated (i.e., moved) by some distance.

**False positive outcome.** The goal of achieving an FP outcome is to introduce a fictitious object that forces the host to

perform dangerous maneuvers (e.g., emergency braking or lane change) to avoid the object. For example, LiDAR spoofing attacks can result in safety-critical incidents, as illustrated with Baidu’s Apollo [2, 40]. Attack success rate (ASR) is defined as the fraction of times a fictitious object is detected over the number of targeted attempts (e.g., number of spoof point clusters), as there could be more than one FP per frame.

**False negative outcome.** The goal of achieving an FN outcome is to eliminate the detection of an existing vehicle such that path planning and control are compromised. Such attacks have even more devastating consequence of causing the host to crash into an unsuspecting object hidden to perception. We similarly define the FN attack success rate (ASR) as the fraction of times an object is missed over the number of attempts (e.g., number of spoof point clusters).

**Naive FP and FN applied to sensor fusion.** Attack success may be greatly reduced with sensor fusion when not all sensors are compromised [8, 31, 40, 41]. Consider the simple context of a camera-LiDAR cascaded fusion under a LiDAR-based attack (e.g., spoofing). We show in Section 5.1 that, with an uncompromised camera, FPs can be identified as detections from LiDAR-only or camera-LiDAR perception that are not consistent with detections from a camera-only perception. Similarly, FNs can be identified by considering the reverse. Even with this simple defense scheme, naive FPs and FNs have limited impact against sensor fusion and can be easily filtered, and we show in Section 5.1 that ASR is reduced to  $< 1\%$  when sensor fusion is employed. Providing detailed analysis of the impact of stealthy (i.e., undetected by integrity/defense) attacks is the focus of Section 5.

**Frustum attack.** Due to the limitations of naive attacks against fusion, we introduce the *frustum attacks* in this work. The motivation follows directly from the relationship between camera and LiDAR data. 2D detections from the camera’s front-view extend a frustum when projected into the 3D LiDAR frame. Due to the reduced dimensionality of the projection, 2D camera detections alone are insufficient to perfectly filter LiDAR points belonging to an object. Therefore, modern perception algorithms employ DNNs to take LiDAR points within a frustum extruded from a 2D region proposal and attribute them to objects. Hence, a (spoof) detection of the sample of spoofed points inside the frustum will appear consistent with the 2D detection from any camera-based perception due to the camera’s inability to resolve range information.

**Translation outcome.** We find that FP and FN outcomes are insufficient to fully capture the effects of the frustum attack. We discover in Section 5 that spoofing LiDAR points in the frustum of an existing object can cause simultaneous FP and FN outcomes, even though the spoofed points are additive to the scene. We call such instances *translation outcomes* as the attacker has created a physical distance between the negated (FN) ground truth 3D bounding box and the resulting detection of the spoofed points (FP). Translation outcomes

Table 1: Parameters for sampling spoof point locations relative to target adversarial location along each coordinate.

Direction	Downrange	Crossrange	Above
Mean (m)	-1	0	0.8
Std. Dev. (m)	0.5	0.5	0.2

retain the same number of objects detected in the scene, which may be desirable to avoid defenses, including the camera-LiDAR cascaded fusion in the paragraph above. Translation outcomes can be similarly devastating by causing emergency braking if objects are moved to front-near positions or cause collision if objects are moved farther away from the host or to a different lane. Section 5.4 further shows that, if exercised over a series of frames, consistent and gradual translation of a bounding box detection would propagate through the AV pipeline, disrupting object tracking, motion prediction, and subsequent path planning, while remaining stealthy. It also may be easier to achieve translation attacks compared to stand-alone FN, as we discuss in Section 5.

## 3.2 Threat Model

### 3.2.1 Environment

We consider an environment where the host AV has multiple sensors. In particular, we consider a monocular camera & LiDAR perception model, similar to [10, 23, 34, 41, 42]. This setup, widely used in real AV systems, is an extension of prior work on AV perception security that consider solely LiDAR [8, 40] or camera [7, 13].

### 3.2.2 Attacker Capability

In this work, we assume that the attacker has no access to the AV’s internal processing and thus can only inject signal along the same physical channels as nominal inputs. Specifically, we consider that the attacker can exercise a LiDAR spoofing attack and has no way to attack the camera. The attacker uses a LiDAR spoofing attack similar to [8, 33, 38, 40] which established how to control the 3D positioning of LiDAR points using a relay and delay system that capitalizes on the original LiDAR emissions. Furthermore, we follow the threat model from [40] which demonstrated feasibility of injecting up to 200 spoof points. While [8, 40] assumed high-precision spoofing where LiDAR points are placed in well-crafted patterns (e.g., outline of a car), we relax this capability in Section 5 and only allow the attacker to place points in a random manner (e.g., normally distributed), which simplifies the attack design compared to the model from [40]; spoofed point distribution parameters are summarized in Table 1.

### 3.2.3 Attacker Knowledge

**System knowledge.** In all cases explored here, the attacker requires no knowledge of the underpinnings of perception, including the machine learning model and perception architecture. Furthermore, the attacker need not have access to existing sensor data, other than what is required in the relay system [33, 38], in order to instantiate these attacks.

**Environmental knowledge.** For the frustum attacks, we assume that the attacker knows the approximate position of the target object so as to obtain a frustum for spoof point placement. This enables FN or translation attack outcomes targeting a particular (valid) object.

## 4 Black-Box Attacks on LiDAR

We first consider general black-box attacks on LiDAR-only perception. To fully evaluate the state of the art, we reproduce the LiDAR spoofing attack from [40] (details are provided in Appendix B). We follow the maximum capability of injecting up to 200 points in patterns of occluded vehicles extracted from KITTI, and use PointPillars [25] for 3D object detection. We sweep number of attack points in sets of 10, from 10 to 200, and carry out 5 attacks in each interval. The simulated spoofed points are appended to the pristine point cloud and fed through the perception pipeline.

We also reproduce the model agnostic defense CARLO [40] (details in Appendix B). CARLO uses the intuition that an FP can be identified because valid LiDAR points will have traveled through the object under test. CARLO is built on the laser penetration detector (LPD) and the free space detector (FSD). We also reproduce LPD, as [40] notes real-time incompatibility of FSD.

### 4.1 Vulnerability to False Positive Outcomes

In [40], CARLO is tested on front-near (5-8 meters) spoofs. This is but a small fraction of the attacker’s space of possible point placement. We show that, *when spoof instances are extended farther from the host, the defense quickly breaks down*. Intuitively, as the range to target increases, the angle subtended by the frustum towards the detection decreases. This leads to a decrease in the number of LiDAR points captured in the frustum as the emitted LiDAR points spread in a spherical pattern. Thus, an increase in range leads to spoofed instances that appear more similar to normal instances under the CARLO hypothesis. The attack effectiveness against CARLO is summarized in Fig. 3, which captures the receiver operating characteristics (ROC) showing that moving 200 spoofed points farther in range deteriorates CARLO classification performance. If true positive rate is fixed at 90%, an attacker can increase attack success rate from less than 5% at front-near to better than 80% at 30 m using the same attack capabilities. We show the change in classification with deterioration of the ROC for 60 spoof points in Appendix C (Fig. 16).

#### 4.1.1 Impact of Multi-Frame False Positive Outcomes

An argument may be made that the impact of FP attacks inserted at larger (i.e., not front-near) distances is minimal. Here, we show that such reasoning is not valid when realistic driving scenarios – i.e., over time (several frames), are considered. The work in [8, 40] motivated front-near injections by their direct (near-term) impact at the driving decisions. With a multi-frame study, *we demonstrate how an attacker can easily*

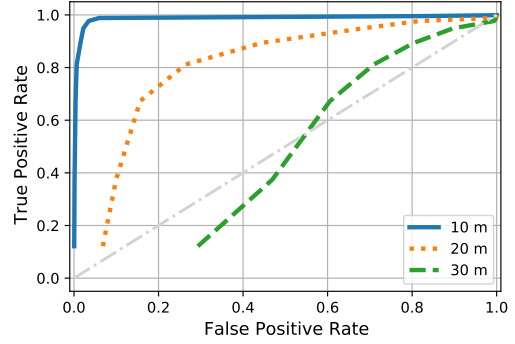


Figure 3: ROC for FP attack on CARLO, 200 points: Attacker breaks the CARLO defense by moving spoofed points farther away from the host AV; e.g., at 30 m distance, the CARLO’s ability to distinguish between detections of valid and spoofed LiDAR point clusters is no better than random guessing.

*achieve high-impact outcomes, endangering vehicle safety, even at larger ranges of false object injection.*

Fig. 4 presents an example of the proof of concept longitudinal (i.e., over time) attack where an attacker spoofs a fake object over multiple frames. Spoofed injections are accepted as valid by the PointPillars + CARLO combination when points are injected at distances of 40 m, 30 m, and 20 m. As shown in Fig. 4, if the attacker inserts the spoof points in consecutive time-frames, the change of position of the injected, falsely detected vehicle results in an estimated (tracked) trajectory of a false vehicle moving directly toward the host with high relative velocity; thus, creating the appearance of impending danger for the host vehicle. Such a scenario triggers breaking and collision avoidance maneuvers even before the false vehicle reaches close range. Only when the spoofed points are injected at 10 m is CARLO able to identify the vehicle as invalid; however, by that point an unnecessary and dangerous avoidance maneuver has already started.

This demonstrates the high-impact nature of spoof point injections outside of front-near. Spoofed objects starting at a distance and moving to front-near locations, rather than spoofing directly in front-near, is a more natural scenario to deceive perception when the full autonomy stack is considered. AVs employ multi-frame object (e.g., vehicle) trackers, estimating object movement to support accurate situational awareness and decision making, which as shown can be exploited by the attacker. Also, when directly injecting in front-near, the object appears to have spawned immediately in front of the host with no trace from tracking; such attacks are invalidated by higher level situational awareness modules. Hence, *multi-frame injections should be an essential part of the attack xplan.*

### 4.2 Vulnerability to False Negative Outcomes

We further discover that CARLO is vulnerable to spoofing attacks for FN outcomes. If CARLO leverages that true objects have few points behind them, then an adversary can

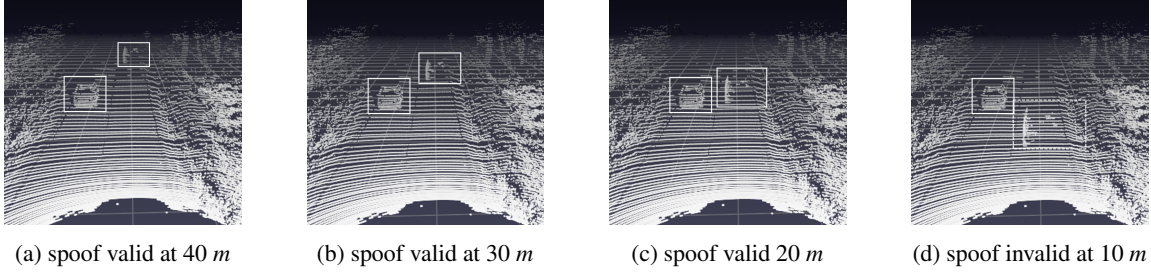


Figure 4: Attacker can emulate a moving spoofed object by varying the distance of injections. The valid object on left is detected alongside the spoofed one on right. Valid object is stationary in the scene while the spoofed appears to be moving towards the host. Only when the spoofed points reach 10 m distance (d) is the spoof object recognized as invalid by the CARLO defense algorithm.

invalidate true objects by injecting points behind them. A benefit of this FN outcome is that it does not require dedicated patterns of injections, unlike the attacks required by [8, 40]. An adversary can inject points in a completely random fashion, as long as they fall within the frustum, to achieve invalidation.

The FN outcomes against CARLO depend on the range to the target to invalidate. This follows from the decrease in the frustum angle with range and the decreasing spatial density of LiDAR points as they propagate spherically. Using a 200-point maximum capability and requiring only random injections, attacks achieve upwards of 40% success at invalidating objects 50 m away. Relaxing the requirement on patterned injections may also allow the adversary to inject. See Appendix C and Figure 17 for more detail.

### 4.3 Impact of Black Box Attacks

We have successfully illustrated that CARLO is insufficient in preventing black box attacks on LiDAR-based perception, as it breaks down with increased distance and builds in vulnerabilities to FN outcomes. Prior to the use of fusion that we outline in the next section, the only alternative was an overhaul of all perception architectures [40], which is costly and undesirable. Moreover, this may not even prevent our frustum attack we show in Section 5, as we discuss in Section 6.4.

## 5 Camera-LiDAR Semantic Fusion Analysis

We first describe how the fusion algorithms inherently defend against LiDAR spoofing attacks from [8, 40] out of the box, resulting in lower ASRs than existing defenses. However, we then demonstrate that, under further scrutiny, *fusion is vulnerable to context-aware black-box LiDAR spoofing attacks*.

### 5.1 Semantic Fusion Guards Existing Attacks

Naive black box LiDAR spoofing attacks (e.g., [40]) will fail to register as valid objects when FPN and FCN are used because those attacks are not consistent with information from the unattacked camera module. As a result, naive attacks will in general not fall within a camera detection and little to no adversarial FPs or FNs will occur. To settle this hypothesis, we use the same attack dataset from [40] and Section 4, and show in Fig. 5 that ASR is diminished to below 1% against both algorithms. Note that even with fixed random seeds, we

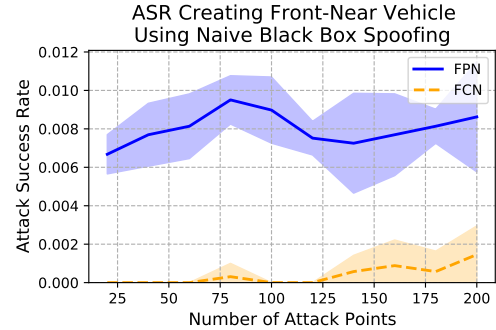


Figure 5: The black box attack from [40] applied naively to FPN and FCN. ASR is diminished to well below 1%, indicating sensor fusion guards against context-unaware attacks. ASR minimally correlated with the number of spoofed points.

still observe natural variation in FPs on the clean dataset, and 1% may be within this natural tolerance. We also find that ASR (Fig. 5) is uncorrelated with the number of attack points.

### 5.2 Frustum Attack Design

Cascaded architectures such as FPN or FCN are attractive from a sensor fusion perspective as they allow for modularity of components, a dramatic reduction in the size of perception data, and they intrinsically provide resilience against naive spoofing attacks. However, here we demonstrate that *semantic fusion is vulnerable to a black-box LiDAR spoofing in the frustum towards existing objects*.

In the analysis that follows, we only consider attacking objects that were strongly detected in the original frame – i.e., since we attack in view (frustum) of existing objects, we do not consider KITTI instances where FPN or FCN perform poorly without attack; such cases would be unfairly easy to attack and would inflate the ASR. We define strong baseline as detections in the original frame with at least 1/2 overlap with ground truth (i.e.,  $\text{IoU} > 1/3$ ), so as to eliminate any doubt that our attack can disrupt even well-performing fusion.

#### 5.2.1 Frustum Attack Motivation

Perception algorithms employ imperfect, often DNN models to identify points belonging to objects. This is true even

with fusion algorithms that filter based on 2D detections from the camera. This forms the basis of why the frustum attack is successful. By specifying spoofing points within a frustum defined by the front-view bounding box towards an object (i.e., the frustum attack), we leverage that, to form detections, the camera-LiDAR fusion algorithms will look within regions of correspondence between 2D image and 3D LiDAR. The frustum attack by definition satisfies camera-LiDAR correspondence by ensuring consistency of spoof point placement with 2D front-view bounding boxes. By injecting close clusters of points towards existing objects, either in patterns of cars as in [40] or in random patterns (e.g., normally-distributed), a camera-LiDAR perception algorithm may be vulnerable to making detections at the spoof point locations instead of (for FPN) or in addition to (for FCN) the original point locations.

### 5.2.2 Attack Implementation

To decouple the performance of a specific 2D detector in our analysis, we consider 2D ground truth detections from the front-view that extrude the frustums, following [34]. We consider a maximum attacker capability of inserting up to 200 spoofed points and the ability to manipulate the range, azimuth, and elevation angles of those points, consistent with capabilities shown in [40]. To improve attack feasibility, we consider normally-distributed random sample point locations to relax challenging placement requirements of previous experiments. We perform a comparison to established patterned injections and find that the attacker does not sacrifice performance when using random sample placement (Appendix D).

### 5.2.3 Example Attack Outcome

We show an example successful frustum attack against FPN in Fig. 6 where 20 spoof points are placed in a normally distributed pattern with a mean location 7 m behind and within the frustum of a target valid object. The target object is composed of 238 points and is at 25 m distance from the host. Even only attacking LiDAR, the frustum attack is successful in obtaining both an FP detection at the spoof point cluster and a simultaneous FN (i.e., missed detection) of the true object. This outcome is a *detection translation*, defined in Section 3. In fact, we find generally that FPN is vulnerable to frustum attacks with detection translation outcomes using far fewer spoof points than are associated with the targeted object’s bounding box (here, 20 vs. 238).

The degree of vulnerability to frustum attacks is explored in detail in next subsections. The far-reaching result of detection translation against FPN using far fewer points than in the valid object is also addressed. We hypothesize that perception algorithms may heavily rely on the ‘shadow region’ for perception, which may give rise to high success levels of frustum attacks (we elaborate on this in Section 6.3). FCN similarly exhibits widespread vulnerability to frustum attacks; however, with far greater vulnerability to FP outcomes in front and behind the target object and less vulnerability to detection translation.

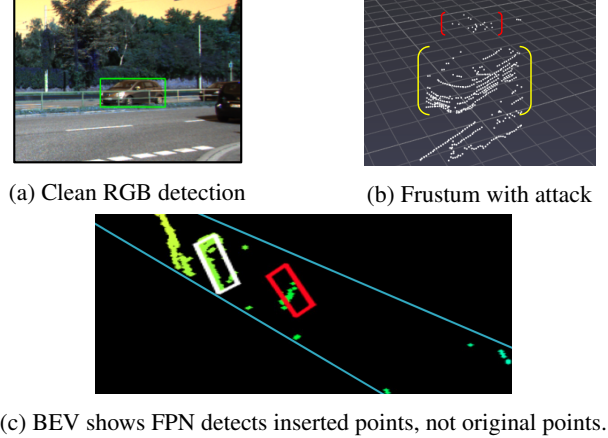


Figure 6: (a) 2D detection yields (b) a 3D frustum of points. Injecting just 20 points in random pattern (bracketed red) deceives 3D object detection, even against a valid object (bracketed yellow) of 238 points; (c) BEV projection of the 3D detection show success of frustum attack with translation outcomes, as the detection (red box) is far from ground truth (white box).

## 5.3 Attack Performance Analysis

### 5.3.1 Motivating example

To motivate the parameter studies, consider an example scene from Fig. 7, where the object is 36 m from the host. On this case, we perform a systematic study of ASR under the frustum attack against FPN. We inject a varying number of spoof points ( $n_i$ ) over multiple trials on  $n_i \in [2, 200]$  and we vary the centroid of the spoof point distribution ( $r_i$ ) on  $r_i \in [r_0, r_0 + 25]$  m, where  $r_0$  is the range to the target vehicle. Experiment outcomes are a set of 3D IoU values comparing the detected object(s) to ground truth. By design, FPN only allows one detection per frustum proposal. Thus, any FP/FN (when FPN is used) is a detection translation outcome. We evaluate the frustum attack as successful with translation outcomes for each combination ( $n_i, r_i$ ) when the resulting detection has no overlap with the ground truth (i.e., IoU = 0).

As shown in Fig. 7b, FPN is vulnerable across a large portion of the attacker capability. There exists a suitable point placement range,  $r_i$ , for all  $n_i > 5$  points and there exists a successful number of injected points,  $n_i$ , for all  $r_i > 4$  m. This phenomenon is not an artifact of selection of the specific scenario. We illustrate the surprisingly high number of objects vulnerable to the frustum attack on FPN and FCN over a large region of the parameter space in what follows.

### 5.3.2 Systematic Performance Study

We consider instances from KITTI where FPN and FCN on the original, clean dataset achieved strong baseline detections (i.e., at least half overlap with ground truth without attack) so as not to capitalize on existing FPs, FNs, or poor performing baseline instances. On each such object, we then run FPN and FCN on the clean points merged with our spoof points from  $n_i \in [2, 200]$  and distance  $r_i \in [r_0 - 20, r_0 + 20]$ .

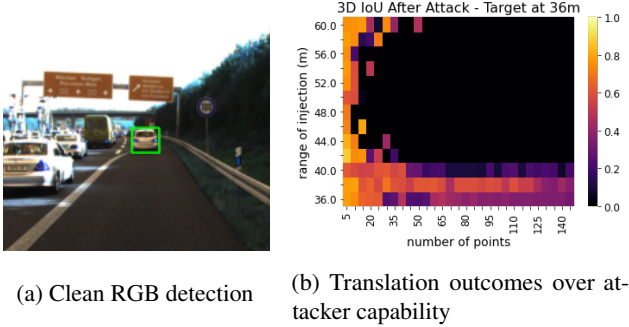


Figure 7: Despite a clean RGB detection (a), a sweep of number of spoof points (b, x-axis) and injection centroid location (b, y-axis) shows that frustum attack is successful against FPN, for many attack parameters. Translation attack outcome is successful when IoU between the detection and ground truth evaluates to 0 (black in (b)). Even less than 10 spoof points create successful attack despite 10x points in original frustum.

**Attackability.** We first define attackability as the ability to find at least one combination of  $(n_i, r_i)$  within established capability (e.g., Fig. 7) that is successful. For FPN, success corresponds to detection translation while for FCN, success is at least an FP and can also be detection translation (i.e., FP + FN). An instance where at least one parameter combination can be found is referred to as ‘*attackable*’.

Fig. 8 shows that the fraction of attackable instances when FPN is used, is strongly correlated with the range to the target vehicle. Similar results hold when FCN is used (Appendix E). As the range increases, the spatial density of LiDAR points decreases due to their propagation in a spherical pattern. This results in fewer points in the bounding box which may lead to increased vulnerability. Also, we notice diminishing returns of attackability by adding more than 60 spoof points, suggesting a convergence of fraction of attackable instances.

**Attackability and bounding box points.** As presented in Fig. 9a, there is a strong correlation between the number of points in the ground truth bounding box and the fraction of instances that can be successfully attacked when FPN is used, suggesting that lower order point sets are more attackable than their higher density counterparts. It is not the case, however, that this greatly limits the attacker. In Fig. 9a, we overlay the proportion of objects that fall within ranges of points per bounding box. This highlights that nearly 60% of the car instances in KITTI contain less than 158 points in the bounding box. Over this space, our frustum attack is nearly 99% effective. Thus, this attack is remarkably successful over the most frequently encountered objects even when the baseline has high performance. Similar results are observed against FCN (Appendix E), with even more success for FP outcomes.

**Minimum attack requirements.** To assuage that we consider an attack capability of up to 200 points, which is more than the number of points in many of these low-point-count,

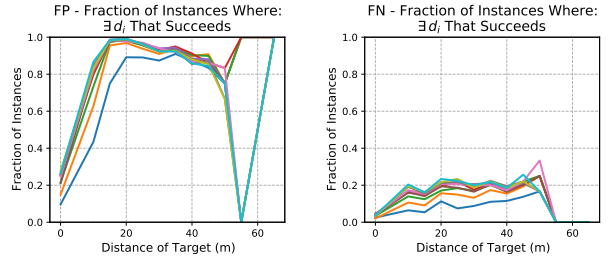
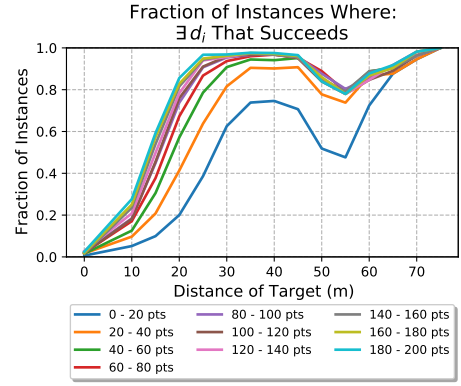
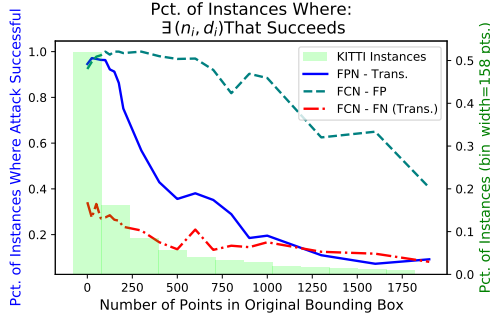


Figure 8: Attackability against FPN and FCN increases sharply for farther targets and with more spoof points, but with diminishing returns to additional points above 60, which is well below maximum attacker capability. Dip in fraction of instances at large range may be artifact of the KITTI dataset.

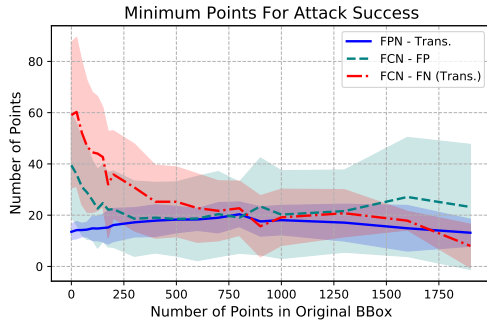
high-frequency instances, we also investigate the minimum number of points for a successful attack (Fig. 9b). We find that, for attackable instances, a surprisingly low number of points – an order of magnitude fewer than the attack capability – are needed to find a placement distance that succeeds. Fig. 9b shows the mean and standard deviation of number of points where some injection distance succeeds, which lies between 10 and 20 points across all attackable KITTI instances. We discover a surprisingly small correlation at high-confidence, (Pearson  $r=0.136$ ,  $p=2.4e-25$ ) – i.e., the number of points in the original bounding box and minimum number of points needed to compromise the fusion are not correlated.

**Attack placement.** The placement of injections is an important element for the success of an attack. We consider an adversary capable of placing the centroid of a spoofed point distribution at certain ranges in a frustum towards a target vehicle. We study the effect of changes in placement on the success of the attack. We furthermore break down the success of each attack by the number of points and by the distance to the target vehicle, and present the results in Fig. 10.

Surprisingly, we find that in each case of number of points and range to target vehicle, *attack success rate against both FPN and FCN peaks near a spoof point injection distance of*



(a) Attack success rate on FPN (translation) and FCN (FP and FN/translation) decrease with the number of points in bounding box, but most natural instances have corresponding high ASR.



(b) Minimum number of spoofed points for successful attack for all outcomes uncorrelated with bounding box points.

Figure 9: (a) [lines, left-y-ax] Fraction of attackable instances strongly correlated with [bars, right-y-ax] number of points in original bounding box. On nearly 60% of KITTI instances, attacker can achieve 99%, 99%, and 38% attack success for translation on FPN, FP on FCN, and translation on FCN. (b) If an instance is attackable, the minimum number of points needed for successful attack is uncorrelated with the number of points in original bounding box (Pearson  $r = 0.136$ ,  $p = 2.4e-25$  for FPN), which benefits the attacker.

9 *m post-target*, as seen in Fig. 10. Distilling such commonality has important consequences for the design of realizable, repeatable, and generalizable attacks. We also discover that, unsurprisingly, ASR increases and overall area under the attack curve increases with both number of attack points and range to the target vehicle (Fig. 10). Intuitively, an increase in each parameter contributes to increases of the fraction of points in the frustum being spoofs.

The ASR deterioration as the injections exceed the location of maximum success is less dramatic for vehicles farther away; i.e., given a fixed ASR objective, the width from lowest to highest injection distances able to achieve at least that ASR increases with increase in range to target vehicle. Appendix F explores this phenomenon – *the attack’s ‘distance margin’*.

## 5.4 Longitudinal Attacks

Isolated instances of spurious attacks on perception will not survive against real AVs. AVs utilize multiple sensors and capture data over a sequence of frames. This helps both to ensure accurate state estimation for path planning and motion prediction and to improve the resiliency of perception to FPs and FNs. With map-aided tracking, AVs can flag FPs that do not comply with semantic map or dynamics information. Tracking over time also builds resiliency to isolated FNs by allowing for coast time in between measurements [6]. Furthermore, a constantly changing environment means that attacks must be easy to find and robust to perturbation.

The frustum attack, with robustness to number of points and distance of injections, as well as success shown with a random spoof pattern, is suitable for temporally consistent spoofing to achieve impact at the tracking level (i.e., over time). Fig. 11 illustrates that an attacker can use his wide distance margin, as presented in Appendix F (Fig. 21), to create longitudinally consistent scenarios even with a-priori selection of parameters. The attacker can then place points at increasing ranges behind the target to create a temporal sequence of attacks.

Consequently, we perform the first temporal security analysis of perception with explicit consideration of vehicle tracking. We present two case studies showing that a frustum attack can be exercised with temporal consistency to disrupt tracking and motion prediction, which then significantly degrades AV control and decision making; thus, endangering the vehicle.

### 5.4.1 Tracking algorithm

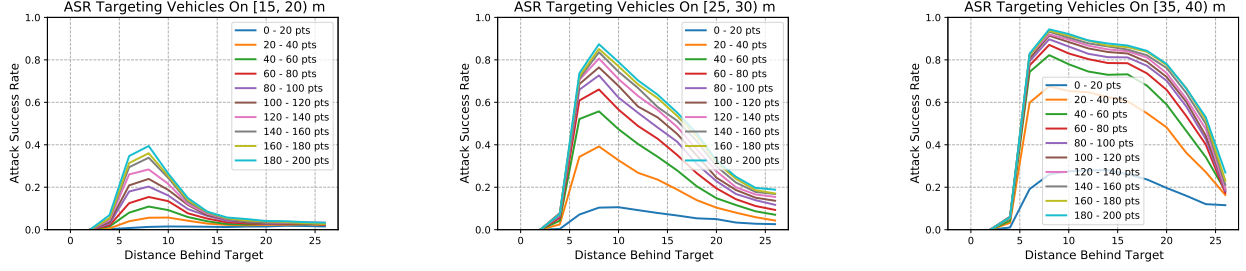
We implement a single-target Kalman filter tracker with position, velocity, and acceleration states according to [6]. We use one tracker per frustum on FPN given the use of ground truth 2D detections and the one detection per frustum specification of FPN. The track (i., trajectory) is predicted forward using a Singer nearly-constant acceleration model and process noise according to [27]. 3D detections from the camera-LiDAR perception algorithm are fed at 5 Hz to the tracking module which tracks box centers over time. We use an industry-standard  $\chi^2$  gating between predicted tracks and timestamped measurements as tracking integrity; this ensures temporal consistency between measurements and prevents unlikely associations from updating tracks. We use the 99% threshold in the  $\chi^2$  gate, specified as

$$0.99 = \Pr(g_k > \tau), \quad \text{where } g_k = z^T Q^{-1} z; \quad (1)$$

here  $\tau$  is the threshold found using the  $\chi^2$  inverse CDF,  $z$  is the innovation between propagated state and measurement, and  $Q$  is the innovation covariance from the Kalman update.

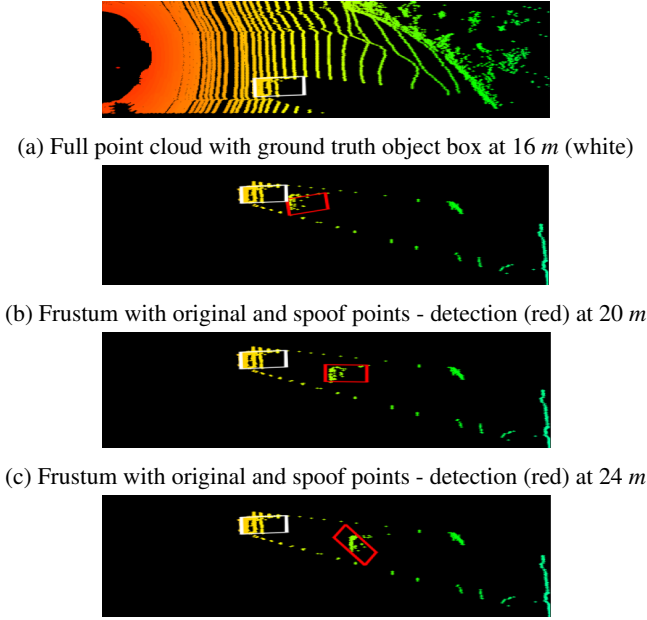
In other words, we neither forced perception to detect our spoofed points nor did we force tracks to accept the resulting detection. We fixed attacker capability at 65 points, which is substantially less than the maximum capability.

For both case studies, RGB and point cloud scenes are shown in Appendix G for better visualization.



(a) ASR on vehicles [15, 20] m peaks at 40% (b) ASR on vehicles [25, 30] m peaks at 90% (c) ASR on vehicles [35, 40] m peaks at 95% with increased width of the region of success

Figure 10: When FPN is used – Attacks are more successful at increased range of target vehicle ((a) vs. (b), (c)). Observation follows naturally from decreased density of points as the LiDAR spreads in 3D. Number of points determines attack success up to a point of minimal return on additional points. For longer range targets (c), attack success over injection distance extends well beyond target range. See Appendix E for the analysis results in vehicles where FCN is attacked.



(a) Full point cloud with ground truth object box at 16 m (white)  
(b) Frustum with original and spoof points - detection (red) at 20 m  
(c) Frustum with original and spoof points - detection (red) at 24 m  
(d) Frustum with original and spoof points - detection (red) at 27 m

Figure 11: (a) Point cloud shows range and scale of target vehicle at 16 m with 492 points in bounding box. Just 65 points are used to alter the target vehicle’s location and achieve detections (translations) at 20 m (b), 24 m (c), and 27 m (d). Movement of bounding box detections in sequential frames can create adversarial false tracks, compromising AV control.

#### 5.4.2 Scenario I: Vehicles at Intersection

We first consider an attacker who desires to create an adversarial track on a crash course for collision with the host. We select an instance for evaluation from KITTI where the target is at 35 m distance. With traffic lanes 4 m wide and vehicles 5 m long, this scenario could represent a large intersection where the cars are initially static.

Due to the fast frame rate of perception, the attacker need only to succeed in attacking over a short time window in

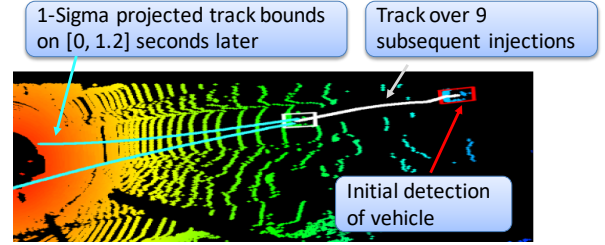


Figure 12: Attacking over multiple frames at attacker-specified distances creates adversarial tracks. Sequences of 65 point spoofs create false detections that are accepted by tracker integrity. Initial detection (red) propagates along white track with time-to-impact with host vehicle predicted 1 s later with small 1-sigma track uncertainty (cyan) near impact.

order for a false track to be created. The attacker chooses to inject 10 sequences of point clusters behind the target which corresponds to 2 seconds of real-time. The attacks increase the distance between successive clusters of points to emulate acceleration of the vehicle towards the host. This is enabled by the wide distance margin from Sec. 5.3.2 (and Appendix F).

Fig. 12 illustrates the BEV of the false track created from this spoofing attack. Eight of the attacker’s ten injections were detected and accepted by the chi-square gate to update the created track. The track has a high degree of certainty about its states with a root-mean-square (RMS) position uncertainty near 0.5 m and RMS velocity uncertainty around 1 m/s.

For path planning, it is essential that each AV understand both the current state of all nearby vehicles as well as their future trajectories, in order to plan a safe path through the environment. After two seconds of injections, a path planner predicts the existing track forward – as seen in Fig. 12 – and the vehicle in front of the host is on a collision course with a time-to-impact of just over 1 s. This triggers dangerous, aggressive and unnecessary collision avoidance maneuver.

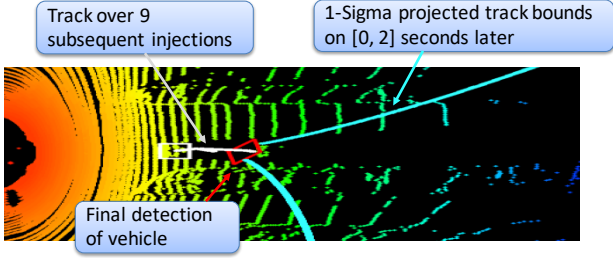


Figure 13: Attacking 5 frames using only 60 points can transform a high-confidence track of a valid vehicle into a low-confidence track with adversarial velocity away from host. One-sigma predicted track bounds suggest vehicle is moving away from host when, in reality, the vehicle and host have no relative velocity (i.e., maintain the same distance). Adversarial track creates problems for path planning and driving safety, as the host vehicle’s adaptive cruise control increases speed.

#### 5.4.3 Scenario II: Highway Following with Adaptive Cruise Control

In the second case study, we consider a similar scenario for a longitudinally consistent attack. We consider highway flow of traffic (e.g., 25 m/s) where adaptive cruise control is using perception to monitor objects and to keep up with the traffic flow. We consider the likely case in which the host AV has already achieved high-precision track on the true vehicle in front. An existing high-confidence, high-precision track is more challenging for an attacker to manipulate. In this case, any dramatic deviation in the location of that object may trigger an alarm or rejection by the  $\chi^2$  integrity monitor, particularly since perception operates at high rate.

Over just five injections which corresponds to just 1 s of real-time, an attacker can manipulate a track with no initial relative velocity (i.e., vehicles traveling in unison) with initial position and velocity uncertainties of 1 m and 1 m/s along each axis. Fig. 13 illustrates that, when path planning updates track prediction for the vehicle in-front, after frustum attack, it appears to travel away at an accelerating rate. This causes an increase in the adaptive cruise control speed because of the apparent increased velocity of the flow of traffic, when in reality, the ground truth vehicle is still traveling with no relative velocity; thus, dangerously approaching the car in front.

**Remarks.** Attacks on perception must propagate into adversarial tracks to impact AVs. Furthermore, we have shown that attacks need not be placed in front-near locations to have high impact. An attacker can use mere seconds of real-time to create false scenarios of predicted collision or accelerate the flow of traffic. In addition, in practice, front-near false-positive attacks as in [8, 40], are likely to be removed by higher level integrity checks, as part of the overall autonomy stack – if no prior track exists, a vehicle suddenly appearing in a front-near position may be just considered as an anomaly, without a prior track. In contrast, attacking at greater distance to objects lever-

ages greater scene complexity and occlusion possibilities. As such, manipulating vehicles at greater distance may be more believable to the AV’s integrity monitoring.

## 6 Discussion and Future Work

We now discuss the robustness of considered attacks and why existing defenses are insufficient at identifying them. We then discuss the implications of the identified vulnerabilities on AV security before introducing avenues for future work.

### 6.1 Intrinsic and Observed Robustness

Robustness to perturbation in attack deployment is important for considering physical realizability of the attack vector. In a dynamic environment where road conditions, weather, or mechanical components can cause small changes in the position of vehicles and alignment of sensors, successful attack vectors must demonstrate robustness.

The design of presented attacks confers a natural robustness, and our empirical results demonstrate additional robustness characteristics. Prior work demonstrated that ASR of naive black box LiDAR spoofing decreased by nearly 50% after applying 20 cm mean L2 norm perturbation at the point level [40]. Our attacks, however, are inherently robust to this level of perturbation; they use a random sample of points with spatial standard deviations above the 20 cm mark along each axis. When evaluating the attack, each attack used a unique sample of point locations. The high success rates prove inherent robustness to changes in point placements.

Additionally, our analysis showed robustness to the number of points and to the placement of the attack along the range dimension. We observe a substantial level of accuracy at low point numbers and results in Fig. 9 show decreasing marginal benefit of adding more than 60 spoofed points. With a maximum attack capability of 200 points, the attacker can afford to be only mildly successful in having spoof points be accepted along the LiDAR channel. The attack distance parameter sweep in Fig. 10 identified that as range of the target vehicle increases, the set of distances usable for the attacks also increases (Appendix F, Fig 21); i.e., successful attacks need not place the points precisely along the range axis.

### 6.2 Single vs. Multiple Objects Per Frustum

FPN and FCN differ primarily in the number of 3D detections allowed per frustum proposal. FPN takes the approach that each proposal from the image have a single 3D detection (i.e., one-to-one correspondence) due to physical occlusion relationships, meaning that any successful attack corresponds to a joint FP and FN outcome (i.e., translation). Importantly, the one object assumption of FPN enhances the resiliency to attack in general, as nearly none of attacks in front of the target object registered as successful. However, translation (FP+FN) of existing detections is a more devastating attack outcome compared to FPs alone.

On the other hand, FCN allows for multiple 3D detections per frustum proposal meaning that FP, FN, and translation

outcomes are all independently possible. We find that this increases the vulnerability to FP attacks. Attacks in front of target objects are dramatically more successful on FCN compared to FPN. Yet, allowing for multiple detections greatly improves the resiliency to FN/translation outcomes with ASR reduced to 25% – see figures in Appendix E.

### 6.3 Vulnerability of the Shadow Region

To understand the differences in outcomes between FPN and FCN, it is important to consider the composition of the frustum. Behind valid objects, there are large shadow regions where no LiDAR points are returned. In fact, the shadow region occupies such a large portion of the frustum as to make DNNs vulnerable to overfitting to this unique feature. An attacker can capitalize on the uniquely defining shadow region of valid objects twofold. First, consider that, by injecting points directly into the shadow region, the injected points leverage the existing shadow region as their own shadow. Second, injecting in the shadow region of a valid object simultaneously perturbs the shadow of that targeted object. Fig. 6b illustrated this outcome with a point cloud visualization where spoof points were injected behind a valid object.

The unique characteristic of the shadow region is a possible explanation for the observed outcomes. First, attacking FPN is only successful with injections behind (i.e., in the shadow of) existing objects (Fig. 10). Second, attacking FPN is successful at translating detections even with dramatically fewer spoof points than belonging to the targeted object (Fig. 9b). Third, while attacking FCN is successful both in front and behind the target, the peak success is higher spoofing behind the target compared to spoofing in front (Appendix E, Fig. 20). Finally, nearly all FN/translation outcomes against FCN occur when points are placed behind the target object (see Appendix E).

### 6.4 Other Defense Algorithms

**CARLO.** We consider the model-agnostic CARLO presented in [40] and analyzed in Section 4. CARLO uses the idea that injected objects do not obey occlusion physics and that with an additive attack model, spoofed objects can be identified when LiDAR points appear to travel through the object. However, the frustum attack retains consistency of the occlusion physics when placed behind the target and capitalizes on the existing shadow. To validate this, we implement CARLO attached to FPN; results provided in Appendix H.

**Sequential view fusion.** We consider sequential view fusion (SVF) as a defense proposed in [40]. Despite the incompatibility of feature-based SVF with point-based FPN/FCN, SVF would still fail to detect attacks on FPN. SVF relies on front-view projections illuminating objects that disobey occlusion relationships. Yet, frustum attacks with translation outcomes have built-in consistency with occlusion relationships by attacking in-view of and achieving FN of a target object.

**GhostBuster.** Finally, the GhostBuster defense extracts features of the shadow region behind object detections, to perform binary classification into valid and invalid instances [16].

The frustum attack is stealthy to GhostBuster, particularly when exercised behind target objects, because it commandeers the shadow region as its own. In the case of FCN where both the original and spoof objects are detected, GhostBuster likely invalidates the original object because its shadow region would be perturbed by our spoofed points.

### 6.5 Limitations and Extensions

**Dataset.** The distribution of objects in the KITTI dataset may not be fully representative of what an AV would see on the road. Thus, future studies ought to extend the dataset and algorithms to address more realistic AV scenarios representing natural sequences of longitudinal data.

**Longitudinal analysis.** Existing case studies in AV security are limited to instances from the KITTI dataset. To give the appearance of a longitudinal scene, we manipulate objects by placing them at different locations in a fixed, static environment. Future work will expand our framework for longitudinal analysis to include multiple target tracking in dynamic environments to facilitate analysis of perception attack impacts on the driving decision (i.e., control) level.

**Shadow region.** The shadow region is one important element for the success of the frustum attacks. Future studies will explore this hypothesis in greater detail to determine if perception DNNs overfit to this unique feature.

**Fusion algorithms.** Our results suggest that fusion at the semantic level is not sufficient in eliminating attacks on perception, contrary to prior hypotheses. These results are important, considering many industry companies publicly report using semantic fusion to handle streams of data from multiple sensors [2, 3]. It remains to be seen whether the same vulnerabilities exist in stronger fusion at the data/feature level.

## 7 Conclusion

We performed the first security analysis of semantic sensor fusion for perception under LiDAR spoofing attacks. While fusion is the only suitable defense against general black-box LiDAR spoofing, we showed it is vulnerable to the frustum attack with random (e.g., normally distributed) spoofing. Across multiple semantic fusion algorithms, we found vulnerability extends to between 70-90% of all cases. We then showed that the number of spoof points needed for a successful attack is independent of the number of points returned by the original object and is more than feasible with existing spoofing devices. We finally presented the first case studies that longitudinally extend attacks on time sequences of perception data.

## Acknowledgements

This work is sponsored in part by the ONR under agreements N00014-17-1-2504 and N00014-20-1-2745, AFOSR under award number FA9550-19-1-0169, as well as the NSF CNS-1652544 award.

## References

- [1] GM Advances Self-Driving Vehicle Deployment With Acquisition of LIDAR Developer, 2017.
- [2] Baidu Apollo, 2021.
- [3] NVIDIA DRIVE, 2021.
- [4] The Evolution of Automated Safety Technologies, 2021.
- [5] Mazen Abdelfattah, Kaiwen Yuan, Z Jane Wang, and Rabab Ward. Adversarial Attacks on Camera-LiDAR Models for 3D Car Detection. *arXiv preprint arXiv:2103.09448*, 2021.
- [6] Samuel S Blackman. Multiple-target tracking with radar applications. *Dedham*, 1986.
- [7] Adith Boloor, Karthik Garimella, Xin He, Christopher Gill, Yevgeniy Vorobeychik, and Xuan Zhang. Attack-ing vision-based perception in end-to-end autonomous driving models. *Journal of Systems Architecture*, 110:101766, 2019.
- [8] Yulong Cao, Chaowei Xiao, Benjamin Cyr, Yimeng Zhou, Won Park, Sara Rampazzi, Qi Alfred Chen, Kevin Fu, and Z Morley Mao. Adversarial sensor attack on lidar-based perception in autonomous driving. In *Proceedings of the 2019 ACM SIGSAC conference on computer and communications security*, pages 2267–2281, 2019.
- [9] Xiaozhi Chen, Kaustav Kundu, Yukun Zhu, Andrew G Berneshawi, Huimin Ma, Sanja Fidler, and Raquel Urtasun. 3d object proposals for accurate object class de-tection. In *Advances in Neural Information Processing Systems*, pages 424–432. Citeseer, 2015.
- [10] Xiaozhi Chen, Huimin Ma, Ji Wan, Bo Li, and Tian Xia. Multi-view 3D object detection network for autonomous driving. In *Proceedings - 30th IEEE Conference on Computer Vision and Pattern Recognition, CVPR 2017*, volume 2017-Janua, pages 6526–6534, 2017.
- [11] Liuyuan Deng, Ming Yang, Yeqiang Qian, Chunxiang Wang, and Bing Wang. CNN based semantic segmen-tation for urban traffic scenes using fisheye camera. In *2017 IEEE Intelligent Vehicles Symposium (IV)*, pages 231–236. IEEE, 2017.
- [12] Mark Everingham, Luc Van Gool, Christopher K I Williams, John Winn, and Andrew Zisserman. The pas-cal visual object classes (voc) challenge. *International journal of computer vision*, 88(2):303–338, 2010.
- [13] Kevin Eykholt, Ivan Evtimov, Earlenice Fernandes, Bo Li, Amir Rahmati, Chaowei Xiao, Atul Prakash, Ta-dayoshi Kohno, and Dawn Song. Robust Physical-World Attacks on Deep Learning Visual Classification. In *Pro-ceedings of the IEEE Computer Society Conference on Computer Vision and Pattern Recognition*, pages 1625–1634, 2018.
- [14] A. Geiger, P. Lenz, C. Stiller, and R. Urtasun. Vision meets robotics: The KITTI dataset. *International Jour-nal of Robotics Research*, 32(11):1231–1237, 2013.
- [15] Ross Girshick. Fast r-cnn. In *Proceedings of the IEEE in-ternational conference on computer vision*, pages 1440–1448, 2015.
- [16] Zhongyuan Hau, Soteris Demetriou, Luis Muñoz-González, and Emil C. Lupu. Ghostbuster: Looking into shadows to detect ghost objects in autonomous ve-hicle 3D sensing. *arXiv*, 2020.
- [17] Andrew Hawkins. Waymo’s autonomous cars have driven 8 million miles on public roads, 2018.
- [18] Jeff Hecht. Lidar for self-driving cars. *Optics and Photonics News*, 29(1):26–33, 2018.
- [19] David Ke Hong, John Kloosterman, Yuqi Jin, Yulong Cao, Qi Alfred Chen, Scott Mahlke, and Z Morley Mao. AVGuardian: Detecting and Mitigating Publish-Subscribe Overprivilege for Autonomous Vehicle Sys-tems. In *2020 IEEE European Symposium on Security and Privacy (EuroS&P)*, pages 445–459. IEEE, 2020.
- [20] Forrest Iandola and Kurt Keutzer. Keynote: small neu-ral nets are beautiful: enabling embedded systems with small deep-neural-network architectures. In *2017 In-ternational Conference on Hardware/Software Code-sign and System Synthesis (CODES+ ISSS)*, pages 1–10. IEEE, 2017.
- [21] Jelena Kocić, Nenad Jovičić, and Vujo Drndarević. Sen-sors and sensor fusion in autonomous vehicles. In *2018 26th Telecommunications Forum (TELFOR)*, pages 420–425. IEEE, 2018.
- [22] Puneet Kohli and Anjali Chadha. Enabling pedestrian safety using computer vision techniques: A case study of the 2018 uber inc. self-driving car crash. In *Future of Information and Communication Conference*, pages 261–279. Springer, 2019.
- [23] Jason Ku, Melissa Mozifian, Jungwook Lee, Ali Harakeh, and Steven L. Waslander. Joint 3D Proposal Generation and Object Detection from View Aggrega-tion. In *IEEE International Conference on Intelligent Robots and Systems*, pages 5750–5757. IEEE, 2018.
- [24] Matti Kuttila, Pasi Pyykönen, Werner Ritter, Oliver Sawade, and Bernd Schäufele. Automotive LIDAR sen-sor development scenarios for harsh weather conditions.

- In *2016 IEEE 19th International Conference on Intelligent Transportation Systems (ITSC)*, pages 265–270. IEEE, 2016.
- [25] Alex H. Lang, Sourabh Vora, Holger Caesar, Lubing Zhou, Jiong Yang, and Oscar Beijbom. Pointpillars: Fast encoders for object detection from point clouds. In *Proceedings of the IEEE Computer Society Conference on Computer Vision and Pattern Recognition*, volume 2019-June, pages 12689–12697, 2019.
  - [26] Phil LeBeau. Waymo starts commercial ride-share service. URL: <https://www.cnbc.com/2018/12/05/waymo-starts-commercial-ride-share-service.html>, 2018.
  - [27] X Rong Li and Vesselin P Jilkov. Survey of maneuvering target tracking. Part I. Dynamic models. *IEEE Transactions on aerospace and electronic systems*, 39(4):1333–1364, 2003.
  - [28] Ming Liang, Bin Yang, Shenlong Wang, and Raquel Urtasun. Deep Continuous Fusion for Multi-sensor 3D Object Detection. In *Lecture Notes in Computer Science (including subseries Lecture Notes in Artificial Intelligence and Lecture Notes in Bioinformatics)*, volume 11220 LNCS, pages 663–678, 2018.
  - [29] Tsung-Yi Lin, Piotr Dollár, Ross Girshick, Kaiming He, Bharath Hariharan, and Serge Belongie. Feature pyramid networks for object detection. In *Proceedings of the IEEE conference on computer vision and pattern recognition*, pages 2117–2125, 2017.
  - [30] Dushyant Mehta, Srinath Sridhar, Oleksandr Sotnychenko, Helge Rhodin, Mohammad Shafiei, Hans-Peter Seidel, Weipeng Xu, Dan Casas, and Christian Theobalt. Vnect: Real-time 3d human pose estimation with a single rgb camera. *ACM Transactions on Graphics (TOG)*, 36(4):1–14, 2017.
  - [31] Miroslav Pajic, James Weimer, Nicola Bezzo, Paulo Tabuada, Oleg Sokolsky, Insup Lee, and George J. Pappas. Robustness of attack-resilient state estimators. In *2014 ACM/IEEE International Conference on Cyber-Physical Systems, ICCPS 2014*, pages 163–174. IEEE, 2014.
  - [32] Nicolas Papernot, Patrick McDaniel, Ian Goodfellow, Somesh Jha, Z. Berkay Celik, and Ananthram Swami. Practical black-box attacks against machine learning. In *ASIA CCS 2017 - Proceedings of the 2017 ACM Asia Conference on Computer and Communications Security*, pages 506–519, 2017.
  - [33] Jonathan; Petit, Bas Stottelaar, Michael Feiri, and Frank Kargl. Remote Attacks on Automated Vehicles Sensors: Experiments on Camera and LiDAR. *Blackhat.com*, 11:1–13, 2015.
  - [34] Charles R. Qi, Wei Liu, Chenxia Wu, Hao Su, and Leonidas J. Guibas. Frustum PointNets for 3D Object Detection from RGB-D Data. In *Proceedings of the IEEE Computer Society Conference on Computer Vision and Pattern Recognition*, pages 918–927, 2018.
  - [35] Charles R. Qi, Hao Su, Kaichun Mo, and Leonidas J. Guibas. PointNet: Deep learning on point sets for 3D classification and segmentation. In *Proceedings - 30th IEEE Conference on Computer Vision and Pattern Recognition, CVPR 2017*, volume 2017-Janua, pages 77–85, 2017.
  - [36] Brandon Schoettle and Michael Sivak. A preliminary analysis of real-world crashes involving self-driving vehicles. *University of Michigan Transportation Research Institute*, 2015.
  - [37] Shaoshuai Shi, Xiaogang Wang, and Hongsheng Li. Pointnet: 3d object proposal generation and detection from point cloud. In *Proceedings of the IEEE/CVF Conference on Computer Vision and Pattern Recognition*, pages 770–779, 2019.
  - [38] Hocheol Shin, Dohyun Kim, Yujin Kwon, and Yongdae Kim. Illusion and dazzle: Adversarial optical channel exploits against lidars for automotive applications. In *Lecture Notes in Computer Science (including subseries Lecture Notes in Artificial Intelligence and Lecture Notes in Bioinformatics)*, volume 10529 LNCS, pages 445–467. Springer, 2017.
  - [39] Vishwanath A Sindagi, Yin Zhou, and Oncel Tuzel. Mvx-net: Multimodal voxelnet for 3d object detection. In *2019 International Conference on Robotics and Automation (ICRA)*, pages 7276–7282. IEEE, 2019.
  - [40] Jiachen Sun, Yulong Cao, Qi Alfred Chen, and Z. Morley Mao. Towards robust LiDAR-based perception in autonomous driving: General black-box adversarial sensor attack and countermeasures. In *Proceedings of the 29th USENIX Security Symposium*, pages 877–894, 2020.
  - [41] James Tu, Huichen Li, Xinchun Yan, Mengye Ren, Yun Chen, Ming Liang, Eilyan Bitar, Ersin Yumer, and Raquel Urtasun. Exploring Adversarial Robustness of Multi-Sensor Perception Systems in Self Driving. *arXiv preprint arXiv:2101.06784*, 2021.
  - [42] Sourabh Vora, Alex H Lang, Bassam Helou, and Oscar Beijbom. Pointpainting: Sequential fusion for 3d object detection. In *Proceedings of the IEEE/CVF Conference on Computer Vision and Pattern Recognition*, pages 4604–4612, 2020.
  - [43] Shaojie Wang, Tong Wu, and Yevgeniy Vorobeychik. Towards robust sensor fusion in visual perception. *arXiv*, 2020.

- [44] Zhixin Wang and Kui Jia. Frustum ConvNet: Sliding Frustums to Aggregate Local Point-Wise Features for Amodal. *IEEE International Conference on Intelligent Robots and Systems*, pages 1742–1749, 2019.
- [45] Yin Zhou and Oncel Tuzel. VoxelNet: End-to-End Learning for Point Cloud Based 3D Object Detection. In *Proceedings of the IEEE Computer Society Conference on Computer Vision and Pattern Recognition*, pages 4490–4499, 2018.

## A LiDAR Spoofing

LiDAR spoofing demonstrations were first reported in [33] where a LiDAR relay systems captured original LiDAR signal from an Ibeo Lux 3; the information was then sent to an attack laser which would emit spoofed LiDAR points consistent with the original signal. Point placement was controlled with a delay component. In addition, the relay attack introduced in [33] used two transceivers – one to receive the original LiDAR signal and send a signal to the second, which controls an attack laser. Two transceivers were used to expand the possible locations the attacker can place the laser. Subsequently, [38] improved the attacker’s capability, specifying the required delay timing for the attacker to place the spoof points anywhere in 3D space. The attack was experimentally validated against a Velodyne VLP-16 LiDAR.

## B Reproducing Black Box Attack

To fully evaluate the existing state of the art, we reproduce the attack on LiDAR-based perception from [40] – we achieved comparable results to the original work. Specifically, we follow their procedure of extracting attack traces from occluded instances found in KITTI. Five attack traces are used to get a distribution at each number of injection points placed in the front-near position. Fig. 14 contains attack success rate for each number of spoof points. The attack achieves near 100% success at just 60 points under the attacks whose goals are FP outcomes.

Similarly, to evaluate the CARLO defense, we reproduce the laser penetration detector (LPD) due to the real-time challenges of the free space detector (FPD) noted in [40] – again, our implementation is on par with the original work. We perform binary classification of valid and invalid objects following the procedure in [40]. A threshold is selected and the empirical cumulative distribution functions (CDFs) illustrated in Fig. 15 indicate that valid and spoof objects are separable with high true positive rate and low false positive rate. Furthermore, Fig. 15 demonstrates that guarding the PointPillars algorithm with CARLO on the original attack vector of front-near injections is able to reproduce the result found in [40].

CARLO is built on two components, the free space detector (FSD) and the laser penetration detector (LPD). FSD ( $f$ ) segments free space voxels in the bounding box and computes

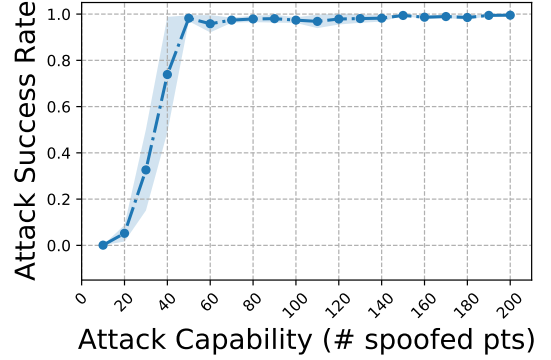


Figure 14: Reproduced attack success rate from [40] that targets PointPillars by injecting occluded instances extracted from the KITTI dataset. As in [40], the attacker can achieve near 100% effectiveness on FP outcomes with just 60 points.

the ratio of free cells ( $\mathbb{1}$  denotes the indicator function) to the bounding box size ( $|B|$ ):

$$f_B = \frac{\sum_{c \in B} \mathbb{1}[c \text{ is free}]}{|B|}; \quad (2)$$

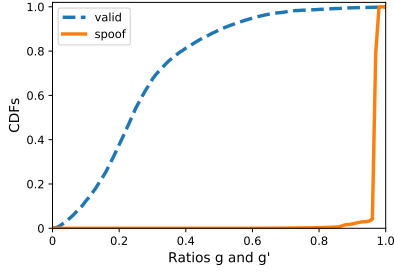
while the laser penetration detector (LPD) ( $g$ ) directly computes the ratio of points behind the bounding box ( $p_i \in B \downarrow$ ) to points in the entire frustum (i.e., the box, as well as behind and before it –  $p_i \in B \cup B \downarrow \cup B \uparrow$ )

$$g_B = \frac{|\{p_i | p_i \in B \downarrow\}|}{|\{p_i | p_i \in B \cup B \downarrow \cup B \uparrow\}|}. \quad (3)$$

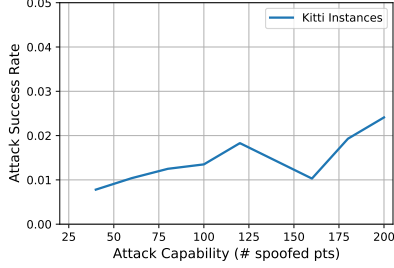
## C Attacking CARLO: Additional Analysis

We provide a brief discussion to further illuminate why the CARLO defense remains vulnerable to FP and introduces vulnerability to FN attacks. In Section 4.1, we demonstrated that CARLO did not adequately defend the models against attacks focused on FP outcomes. There, we described that CARLO breaks down with increased distance of spoofed objects injected by the attacker. This is because the size of the frustum subtended by a detection decreases with distance and therefore fewer original points will be captured within the detection frustum as the spoofed object distance increases. This causes a decrease in the LPD statistic of spoofed objects, making them appear more similar to valid objects.

Here, we show how this change in captured points changes the classification problem. Fig. 16 demonstrates the effect of moving spoof injections on the binary classification problem via the receiver operating characteristics (ROC) curve. The ROC curves show a dramatic decrease in classifier performance as the distance of spoofed injections increases. In fact, with the maximum attacker capability of 200 points, using LPD to detect spoofs at 30 m distance is no better than the



(a) Empirical distributions of LPD statistic for valid (blue) and spoof (orange) are separable



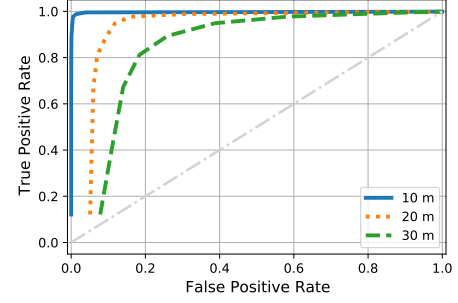
(b) CARLO-guarded PointPillars has low ASR

Figure 15: With our implementation of CARLO, we reproduce the CARLO’s LPD defense results from [40]. For example, results show that: (a) valid (blue) and spoof (red) objects are separable by a threshold on the ratio of points behind bounding box to points in frustum; (b) using the defense to guard PointPillars reduces attack success rate to below 5%.

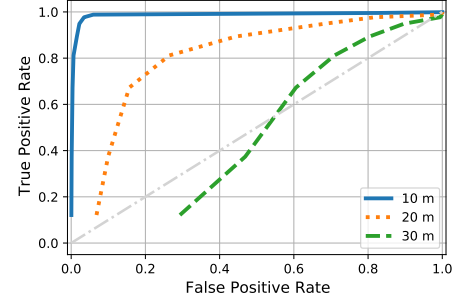
random guessing classifier. This is a direct result of the decrease in the frustum size and fewer original points captured as the spoof objects move farther away.

Similarly, we show how spoofing points behind valid objects can induce FN (i.e. invalidation) outcomes. Adding points behind valid objects increases the CARLO statistic, making the valid objects appear more similar to the spoof class. A benefit of the FN outcome against CARLO is that spoof points can be placed uniformly at random behind a valid object, in order to invalidate it, which may be easier for an attacker to realize. We use 200 points to achieve invalidation of objects at varying distances. The classification performance quickly deteriorates, as presented in Fig. 17, as the range to those targeted objects increases as a direct consequence of the spherical LiDAR emission and decreased subtended frustum angle.

Finally, in Section 4.1.1, we demonstrate how longitudinal spoofing on LiDAR-based perception can have high impact, even if vehicle injections are farther than front-near position. In Section 5.4, we extend this concept to a tracking module using semantic fusion perception. To supplement the visualization of the case study attack on LiDAR-based perception with the CARLO defense, Fig. 18 provides front-view camera images with LiDAR returns and object detections overlaid.



(a) ROC with 60 spoof points



(b) ROC with 200 spoof points

Figure 16: Increasing the distance of spoof points is enough to deteriorate CARLO’s ability to guard LiDAR-based perception algorithms – analysis for 200 and 60 spoofed points. For example, with 200 spoof points, CARLO is no better than random guessing at a distance of 30 meters.

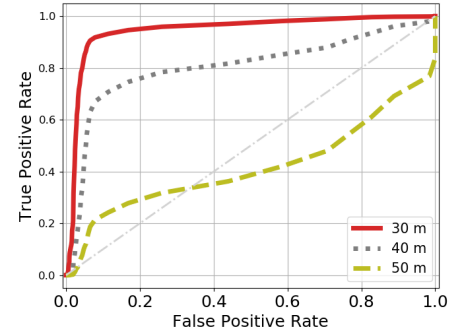


Figure 17: Attacker uses CARLO to obtain false negative (i.e., invalidation) outcomes against valid objects in the scene using 200 uniformly random spoofed points. FN attacks are more successful at increased range to target, capitalizing on the spherical emission pattern of LiDAR points.

These are associated with the point cloud visualizations in Fig. 4. Color indicates range to point.

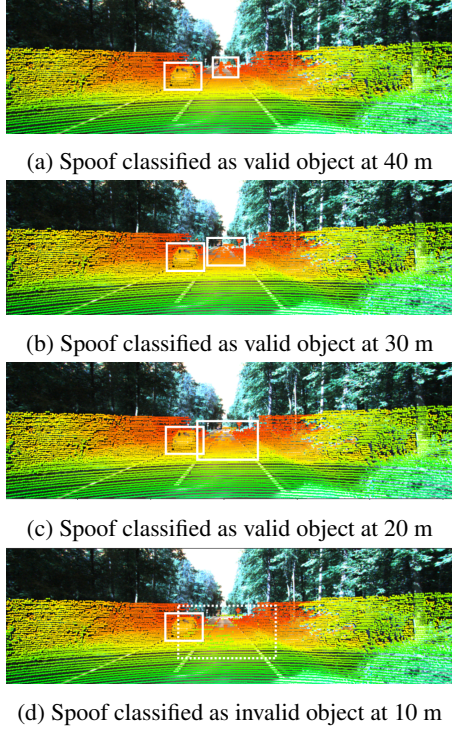
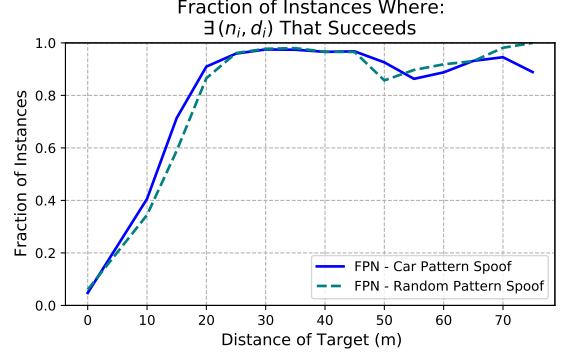


Figure 18: Front view projection of the attacker emulating a moving spoofed object – the figure is associated with the point cloud visualizations in Fig. 4. Left detection is a real object, right detection is a spoofed object. The attacker spoofs over multiple frames to create an adversarial velocity on the spoof object. Only when the object reaches 10 meters distance it is classified as fake by the CARLO defense.

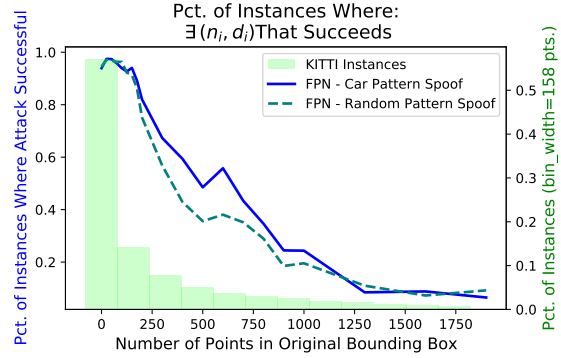
## D Comparing Spoof Point Placement

In Section 5.3.2, we outline the performance of the frustum attack on semantic multi-sensor fusion. Here, we illustrate that placing spoofed points in a normally-distributed pattern has attack success on-par with the use of occluded car patterns when attacking Frustum PointNet. Prior security analyses required either white-box access to optimize for placement of spoof points [8] or carefully crafted spoof point placement in the pattern of real vehicles [40]. Our result improves the feasibility of LiDAR-based spoofing, as a normally distributed pattern does not require unrealistically careful placement of spoof points and improves robustness to small perturbations, as each random point cluster we test is a different sample of points.

To simulate the performance of a physical spoofing device emitting in a normally-distributed pattern, we draw a sample of point locations from a multivariate Gaussian with moments in Table 1. We rounded the moments to the nearest 10 cm to make it clear that, to achieve high attack success, *the distribution parameters need not be unrealistically precise or tailored to any particular attack instance*. Intensity values on



(a) Comparison of patterns against distance to target.



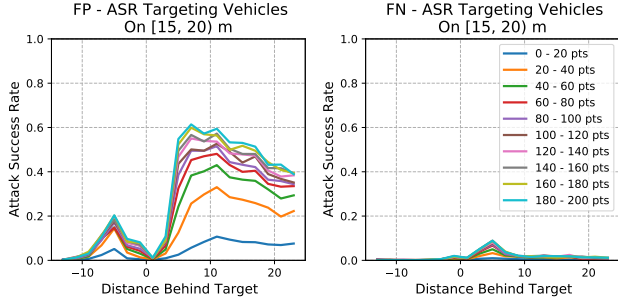
(b) Comparison of patterns against points in targeted bounding box.

Figure 19: A comparison of strategies for spoofing points illustrates that, under spoofed points in a Gaussian random sample pattern and occluded car pattern (a) the fraction of attackable instances is nearly equivalent and (b) the dependence of attackability on points in target bounding box is nearly equivalent.

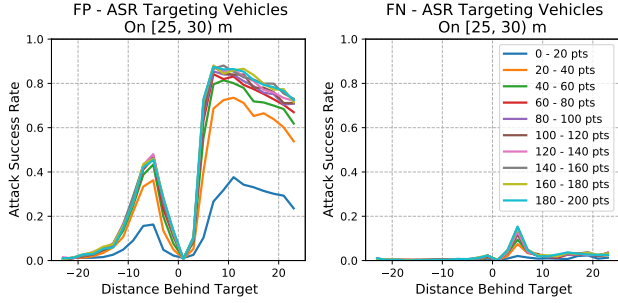
the LiDAR points are drawn with replacement from nearby point instances in the scene to simulate signal attenuation that would be seen in a physical environment.

To compare attack success of the normally-distributed pattern with the carefully crafted spoof points, we first provide a comparison of the fraction of instances where an attack succeeds using both methods (seen Fig. 19a). As can be observed, it is difficult to distinguish between the performance of the two methods (random points vs. car-pattern).

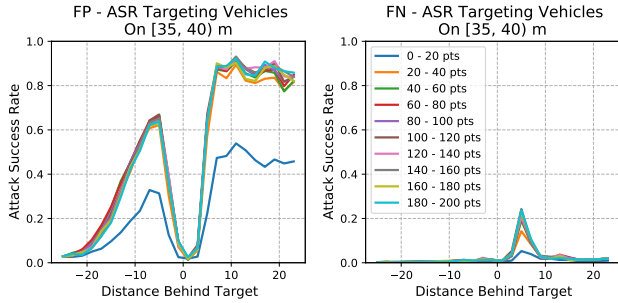
We furthermore provide an analysis of the attackability as a function of the number of points in the target objects' bounding box, in Fig. 19b. We defined attackability as the ability to find an attack that succeeds within the attacker-specified capabilities. Qualitatively, the performance of both methods is similar with a small benefit of car patterned injections at medium range.



(a) (FCN) ASR on vehicles [15, 20] m peaks near 60% for FP (left) and 8% for FN (right)



(b) (FCN) ASR on vehicles [25, 30] m peaks near 85% for FP (left) and 18% for FN (right)



(c) (FCN) ASR on vehicles [35, 40] m peaks near 90% for FP (left) with increased width of the region of success, and 21% for FN (right)

Figure 20: When FCN is used – Attacks are more successful at increased range of target vehicle ((a) vs. (b), (c)). Observation follows naturally from decreased density of points as the LiDAR spreads in 3D. Number of points determines attack success up to a point of minimal return on additional points. For longer range targets (c), attack success over injection distance extends well beyond target range. Unlike on FPN, attack success is substantial when attacking in front of the target.

## E Attacking FCN - Additional Results

Similar to Fig. 10 in Section 5.3.2, we analyze the effect of changing spoof placement for FP and FN/translation outcomes when FCN is used; the results are summarized in Fig. 20. Attack success when injecting behind a target object for FP outcomes peaks at 9 meters, similar to attacks against

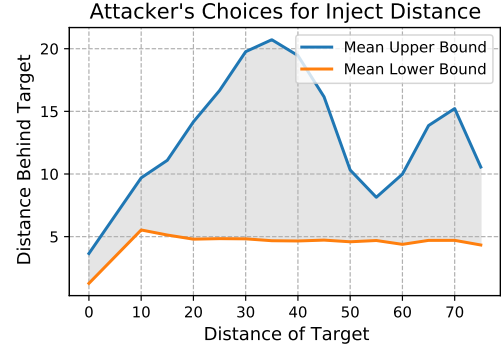


Figure 21: Attacker has margin (anywhere in the gray region) of successful distance for frustum attack spoof locations for all target distances against FPN. Margin increases with distance to target until a dip occurs at medium-range objects.

FPN. Attack success for FN/translation outcomes peaks at 5 meters behind target where the only successful attacks exist. Recall that FCN allows for multiple detections within a frustum, so obtaining a strictly FN/translation outcome is a more challenging feat compared to translation outcomes on FPN. Notably, we use 'FN/translation' because, while we observe that all FN outcomes obtained thus far on FCN have a corresponding FP (i.e., are a translation), unlike on FPN where there is always a detection per frustum, there is no guarantee of a detection on FCN; thus, there may be cases of isolated FN without associated FP that we have not observed.

## F Attacker's Distance Margin

We continue to explore the attacker's distance margin, first discussed in Section 5.3.2. For a fixed distance to a target object, we sweep the number of points and inject distance over the attacker parameter space. We then find the mean lower and upper bounds on inject distance where an attack registers as successful. Due to the smoothness of the convex hull of attack parameters observed from Fig. 7, each distance in between lower and upper bounds is also likely to be successful.

Distance margin results for FPN are presented in Fig. 21. In general, the lower bound is nearly constant at 5 m beyond the target vehicle. The upper bound initially increases with distance of the target; however, there is a noticeable dip that we hypothesize is a statistical artifact of the small size of KITTI but should be subject to further investigation. The large distance margin means the frustum attack is robust to changes in spoof point placement and that the attacker has a large area over which to achieve high-impact longitudinal outcomes.

## G Tracking Case Study Visualization

Supplementary visualizations for the tracking case studies presented in Section 5.4 are included in Fig. 22 and 23.

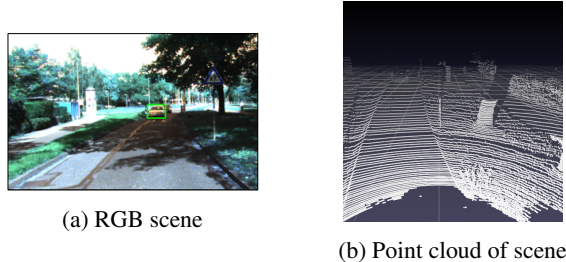


Figure 22: Supplementary visualization for the first tracking (i.e., longitudinal) security analysis, described in Section 5.4.2.

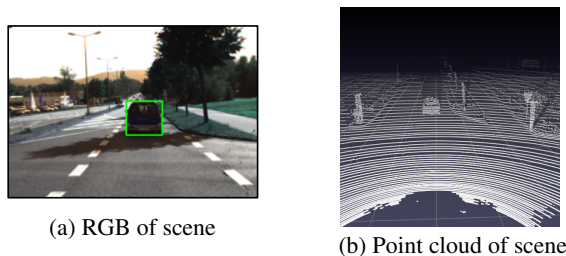


Figure 23: Supplementary visualization for the second tracking (i.e., longitudinal) security analysis, described in Section 5.4.3.

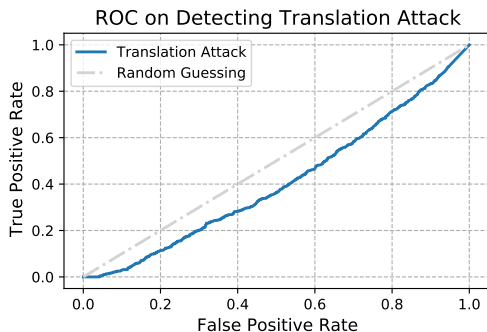


Figure 24: Receiver operating characteristics (ROC) of using CARLO to distinguish between clean and frustum attack instances. CARLO defense performs worse than the random guessing classifier, demonstrating that the frustum attack, with its semantics-preserving formulation, is not detectable by existing defenses.

## H CARLO Fails on Frustum Attack

In Section 6.4, we outline an intuitive explanation why CARLO fails to detect the frustum attack. Again, the considered spoofing attacks obey occlusion relationships by attacking in view of an existing object and are particularly consistent when attacking behind valid objects. Here, we provide quantitative results showing that the LPD portion of CARLO fails to detect the frustum attack. We choose not to implement FSD due to incompatibility of FSD with real-time

systems [40]. We take 1000 samples of where an attack is successful against FPN and compute the LPD statistics on both the clean and attacked version according to [40]. Fig. 24 presents receiver operating characteristics (ROC) that capture performance on the binary classification problem. Results show that detections from the frustum attacks are even more ‘natural’ than the unattacked case, under the CARLO hypothesis, as CARLO is strictly worse than the random guessing classifier for all possible thresholds.